EVALUATION OF A NEW GRIDDING METHOD FOR FULLY 3D DIRECT FOURIER PET RECONSTRUCTION BASED ON A TWO-PLANE GEOMETRY

F Ben Bouallègue, JF Crouzet, and D Mariano-Goulart

_____

Abstract

This study investigated how the choice of fixed planes for the representation of the projection data of a cylindrical PET scanner simplifies the frequency interpolation required by the 3D Fourier slice theorem (3D-FST). A new gridding algorithm based on a two-plane geometry and requiring only 1D interpolations in the Fourier domain was compared with the direct implementation of the 3D-FST. We show that the use of two orthogonal planes leads to signal to noise ratios similar to those achieved with the 3D-FST algorithm from projection data acquired with up to two times more count rates, while the resolution remains similar.

Keywords

Direct Fourier methods, gridding algorithms, interpolation, PET, 3D reconstruction.

1. Introduction

The widespread clinical use of whole-body fully three-dimensional Positron Emission Tomography scanners (3D-PET) has made necessary accurate reconstruction algorithms whose execution time is similar to the time needed to record the next set of projection data (i.e., the next bed position). Moreover, the need to decrease patient irradiation or speed up the acquisition procedure (for dynamic PET, for instance) has stimulated research to optimize the signal to noise ratio in the reconstructions.This has led to the development of reconstruction methods that are theoretically able to take advantage of the redundancy of 3D-PET projection data.

Significant improvements in the reconstruction speed can be achieved using exact or approximate algorithms that sort the 3D projections into a 2D dataset containing one sinogram for each transaxial slice to be reconstructed. The resulting sinograms are processed using conventional 2D tomographic reconstruction algorithms. Among these so-called rebinning methods, the approximate Fourier rebinning algorithm (FORE) allows a significant speed-up in the reconstruction and provides a reliable alternative to 3D reconstruction algorithms in routine clinical settings [1-8]. However, the FORE algorithm is based on an approximation that breaks down when the axial aperture of the scanner increases.

Following the pioneering research of Orlov [9-10], most noteworthy contributions toward a fully 3D tomographic reconstruction procedure have been inspired by the search for a generalization of the usual 2D reconstruction algorithms [11]. 3D versions of iterative algorithms (such as 3D-OSEM) can provide accurate volume reconstructions and do not require shift-invariance of the projection data. However, in spite of the recent works that intended to speed up the 3D back- and forward-projection operators [12- 15],

the intensive use of these procedures by the iterative algorithms makes them relatively slower compared with other 3D reconstruction methods such as direct Fourier methods.

Other 3D reconstruction algorithms are based on the Fourier slice theorem and require shift-invariance of the projection data. This is generally not the case for the usual cylindrical PET scanners, since some line integrals characterized by a particular direction may be measured for points that are located near the center of the field of view but not for points located at the border of the field of view. The shift-invariance of the projection data can be achieved by forward-projecting a first estimate of the unknown radioactive distribution, which is reconstructed from those projection views that are complete. Among these algorithms, the 3D filtered back-projection (3D-FBP) algorithm has been studied extensively [16-19]. Like other algorithms using back-projections (and forward-projections to estimate the missing projection data), the 3D-FBP remains much more time-consuming than 2D slice-by-slice algorithms or 3D direct Fourier methods.

Alternatively, the 3D Fourier slice theorem makes it possible to compute the 3D Fourier transform of the unknown radioactive distribution from the set of 2D Fourier transforms of the projection data [20-25]. These direct Fourier methods (DFM) have the potential to substantially speed up the reconstruction process (when a simple 3D interpolation procedure is used with no oversampling, the processing time is 28 times faster compared with a back-projection procedure [22]) and are likely to produce accurate and high-speed 3D reconstructions, provided that the interpolation accuracy in the Fourier domain is controlled. The complex interpolation in the frequency space required by DFM can be controlled by an increase in the sampling frequency, achieved by zero padding in the projection data and the image [26]. More recently, gridding interpolation with proper interpolating window (e.g., a modified Kaiser-Bessel window) and data weighting functions has been proposed to optimize the interpolation process [27-36].

Besides this progress in the interpolation process, some improvement in the accuracy of DFM for 3D-PET may be found in the better adjustment of the grids that are used to process the unknown 3D distribution of radioactivity from the 2D projection data in the Fourier space. The reduction of the interpolation dimensionality for DFM is based on a principle similar to that of the linogram method that was first developed by Edholm et al. [37,38]. The first step was achieved by replacing the 3D interpolation (required by the Fourier slice theorem) by 2D interpolations within the transverse planes. This was enabled by conserving the axial sampling of the ring PET scanner geometry [22,31,36]. Similarly, Brasse et al. proposed a fast and accurate 3D back-projection algorithm for planar detector arrays [15]. This so-called planogram method succeeded in simplifying and accelerating the back-projection procedure by applying Fourier transforms in the natural acquisition geometry of planar detectors and using only 2D interpolations. Brasse et al. [15] noted that the planogram method can be used to design forward-projection procedures (using only 1D interpolations), which are interesting, for example, to compute the missing projection data in a cylindrical PET scanner. However, they did not exploit the planogram method to simplify the interpolation step in direct Fourier methods, nor did they propose any validation study for this class of 3D reconstruction methods. A few months later, a theoretical paper emphasized the interest of processing the projection data of a cylindrical PET scanner on a single fixed transversal plane to implement direct Fourier reconstruction methods using 1D interpolations in the Fourier space only [39]. After evaluation, the proposed method appeared however to be badly designed for the processing of classical 3D PET data acquired at low tilt angles.

To complement the works dedicated to the choice of an interpolation process, the present study investigated how the choice of specific fixed planes in the representation of the projection data of a cylindrical PET scanner can improve the accuracy of the interpolation procedures in the frequency space

that are required by direct Fourier methods. First, we present a theoretical framework for 3D direct Fourier methods that naturally introduces two algorithms with the property of requiring only a 1D interpolation instead of the complex 3D interpolation required by the direct implementation of the Fourier slice theorem. Using the same interpolation procedure, the resolution and noise properties of an algorithm using two orthogonal projection planes are compared with those of the direct computation of the Fourier slice theorem. Last, the reconstruction of PET data acquired in routine clinical settings is shown to illustrate and compare the qualities of these algorithms.

2. Unified framework for direct 3D Fourier methods with an arbitrary projection plane in PET

We addressed the problem of computing an unknown activity distribution f from its shift-invariant projections acquired using a cylindrical PET scanner. Let us consider a shift-invariant projection recorded along a direction w on an arbitrary plane $u_3^\perp$ passing through the origin (figure 1). Consider an orthonormal basis (O, u_1, u_2) of the plane $u_3^\perp$ such that $u_1 \wedge u_2 = u_3$, where $\wedge$ denotes the usual cross product. (O, u_1, u_2, u_3) is an orthonormal basis of the 3D space.
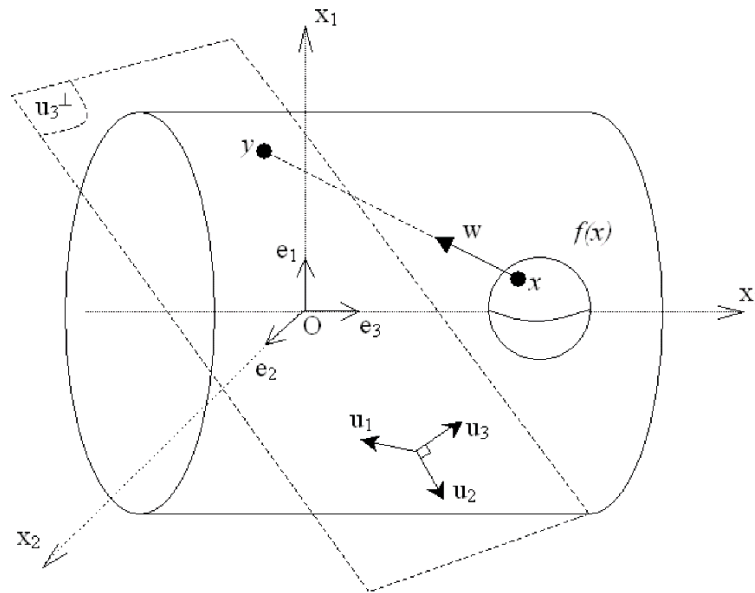

Figure 1. Illustration of the projection of an unknown 3D radioactive distribution $f(x)$ onto a projection plane $u_3^\perp$.

We denote $U = [u_1 \; u_2 \; u_3]$, the matrix of the linear application that maps the canonical basis (O, e_1, e_2, e_3) into (O, u_1, u_2, u_3). Denoting ${}^t(.)$ the transpose, the projection computed at the point $y \in u_3^\perp$, whose coordinates are ${}^t(y_1, y_2, 0)$ in the basis (O, u_1, u_2, u_3), is

$$p_w(y_1, y_2) = \int_R f(Uy + tw)dt . \qquad (1)$$

Let us take the 2D Fourier transform $\hat{p}_w$ of p_w,

$$\hat{p}_w(\xi_1,\xi_2) = \iint_{R^2} p_w(y)\, e^{-2i\pi\xi.y}\, dy = \iiint_{R^2\,R} f(Uy+tw)\, e^{-2i\pi\xi.y}\, dy\, dt \,, \text{ where } \xi = {}^t(\xi_1,\xi_2,0). \tag{2}$$

Denoting $z={}^t(y_1,y_2,t)$, we have $Uy+tw=[u_1 \; u_2 \; u_3]y+tw=[u_1 \; u_2 \; w]z=Az$, where A is the matrix:

$$A=[u_1 \; u_2 \; w]. \tag{3}$$

Let us proceed to the change of variable $x={}^t(x_1,x_2,x_3)=Az$. The Jacobian of this transformation is

$$\alpha = |det(A^{-1})| = \frac{1}{|det(A)|} = \frac{1}{|(u_1 \wedge u_2).w|} \,, \text{ that is } \alpha = \frac{1}{|u_3.w|} \,. \tag{4}$$

As $y.\xi=z.\xi$ and $dydt=dz=\alpha dx$, equation (2) leads to

$$\hat{p}_w(\xi_1,\xi_2) = \iiint_{R^3} f(Az)e^{-2i\pi z.\xi}\, dz$$

$$= \alpha \iiint_{R^3} f(x)e^{-2i\pi A^{-1}x.\xi}\, dx$$

$$= \alpha \iiint_{R^3} f(x)e^{-2i\pi x.\,{}^tA^{-1}\xi}\, dx. \tag{5}$$

Thus one obtains a closed-form formula for the general reconstruction problem using an arbitrary projection plane:

$$\hat{p}_w(\xi_1,\xi_2) = \alpha\, \hat{f}({}^tA^{-1}\xi), \tag{6}$$

where α is the Jacobian defined by equation (4). This formula makes it possible to compute the 3D Fourier transform of the unknown radioactive distribution $\hat{f}$ from the 2D Fourier transform of the projections $\hat{p}_w$ along a direction w onto a plane $u_3^{\perp}$ passing through the origin.

3. Deriving reconstruction algorithms

Having described a general framework for Fourier-based reconstruction methods using arbitrary projection planes, we turned our attention to some choices of projection planes that are likely to simplify the interpolation procedure required by equation (6) to compute the radioactive distribution $\hat{f}$ from the projection data $\hat{p}_w$. The manner by which the original projection data from a usual cylindrical PET scanner were re-sampled into the specific projection planes is described in the next paragraph, together with other numerical issues. Recalling that $w={}^t(\cos\theta\cos\varphi,\cos\theta\sin\varphi,\sin\theta)$, where θ and φ are the Euler angles, we now derive different reconstruction schemes from equation (6).

3.1. One-plane method: projection on a single transaxial plane

Let us choose the transaxial plane (O,x_1,x_2) to collect the projection data. Thus $(u_1,u_2,u_3)=(e_1,e_2,e_3)$ and equation (3) leads to

$$A = \begin{pmatrix} 1 & 0 & w_1 \\ 0 & 1 & w_2 \\ 0 & 0 & w_3 \end{pmatrix} \qquad (7)$$

The Jacobian defined in (4) is $\alpha = 1/|w_3| = 1/\sin\theta$ (for $\theta \in [0, \pi/2[$), so that

$$^t A^{-1} = \begin{pmatrix} 1 & 0 & 0 \\ 0 & 1 & 0 \\ -w_1/w_3 & -w_2/w_3 & 1/w_3 \end{pmatrix}. \qquad (8)$$

Thus equations (7) and (8) lead to the final reconstruction formula for the one-plane method:

$$\hat{p}_w(\xi_1, \xi_2) = \frac{1}{\sin\theta} \hat{f}(\xi_1, \xi_2, -(\xi_1\cos\varphi + \xi_2\sin\varphi)/\tan\theta). \qquad (9)$$

The reconstruction process corresponding to equation (9) was first proposed in [39] for 3D PET. However, because of the $1/\sin\theta$ factor that tends to explode at low tilt angles, the one-plane method is badly designed for the processing of 3D data acquired with classical PET scanners and may be of interest only in the case of large aperture scanners providing 3D projections with high tilt angles. Thus, this method will not be considered further.

3.2. Two-plane method: projection on two orthogonal planes

Let us choose the coronal and sagittal planes (O, x_2, x_3) and (O, x_1, x_3) to collect the projection data, depending on the value of φ. For a given projection characterized by w, the plane that is chosen to process these projection data is the one onto which the norm of the projection of w is the smallest. In other words, the plane (O, x_2, x_3) is used if $|\varphi| < \frac{\pi}{4}$ or $|\varphi| > \frac{3\pi}{4}$; otherwise, the plane (O, x_1, x_3) is used to process the projection data. Using the plane (O, x_2, x_3), we have $(u_1, u_2, u_3) = (e_2, e_3, e_1)$, so that

$$A = \begin{pmatrix} 0 & 0 & w_1 \\ 1 & 0 & w_2 \\ 0 & 1 & w_3 \end{pmatrix}. \qquad (10)$$

The Jacobian is $\alpha = 1/|w_1| = 1/|\cos\theta\cos\varphi|$, and

$$^t A^{-1} = \begin{pmatrix} -w_2/w_1 & -w_3/w_1 & 1/w_1 \\ 1 & 0 & 0 \\ 0 & 1 & 0 \end{pmatrix} \qquad (11)$$

Thus we obtain, using equation (6),

$$\hat{p}_w(\xi_1, \xi_2) = \frac{1}{|\cos\theta\cos\varphi|} \hat{f}(-\xi_1\tan\varphi - \frac{\xi_2}{\cos\varphi}\tan\theta, \xi_1, \xi_2). \qquad (12)$$

Let us now use the plane (O, x_1, x_3) so that $(u_1, u_2, u_3) = (e_1, e_3, -e_2)$:

$$A = \begin{pmatrix} 1 & 0 & w_1 \\ 0 & 0 & w_2 \\ 0 & 1 & w_3 \end{pmatrix}.$$ (13)

The Jacobian is $\alpha = 1/|w_2| = 1/|\cos\theta\sin\varphi|$, and

$$^tA^{-1} = \begin{pmatrix} 1 & 0 & 0 \\ -w_1/w_2 & -w_3/w_2 & 1/w_2 \\ 0 & 1 & 0 \end{pmatrix}.$$ (14)

Thus equation (6) gives:

$$\hat{p}_w(\xi_1,\xi_2) = \frac{1}{|\cos\theta\sin\varphi|} \hat{f}(\xi_1, -\frac{\xi_1}{\tan\varphi} - \frac{\xi_2}{\sin\varphi}\tan\theta, \xi_2).$$ (15)

Depending on the value of φ, equations (12) and (15) can be used as a reconstruction algorithm to build up $\hat{f}$.

3.3. FST method: direct use of the Fourier slice theorem

To use the Fourier slice theorem as a reconstruction scheme, one has to consider $w^\perp$ as the plane where the projection data are processed. Thus $u_3 = w$, and we can choose the unitary vectors

$u_1 = {}^t(\sin\theta\cos\varphi, \sin\theta\sin\varphi, -\cos\theta)$, and $u_2 = {}^t(-\sin\varphi, \cos\varphi, 0)$, so that $u_1 \wedge u_2 = w$.

Then the Jacobian defined in (4) is $\alpha = 1/|w.w| = 1$, and $^tA^{-1} = A$ as A is an unitary matrix exchanging the two bases. Hence the general equation (6) leads to the classical reconstruction formula corresponding to the 3D Fourier slice theorem: $\hat{p}_w(\xi_1,\xi_2) = \hat{f}(A\xi)$, that is:

$$\hat{p}_w(\xi_1,\xi_2) = \hat{f}(\xi_1\cos\varphi\sin\theta - \xi_2\sin\varphi, \xi_1\sin\varphi\sin\theta + \xi_2\cos\varphi, -\xi_1\cos\theta).$$ (16)

4. Numerical implementation

Some points regarding the numerical implementation of the two-plane method need to be detailed:

The geometric characteristics of the scanner are the following: L is the axial FOV, R the radial FOV, and $\delta_{max} = \tan\theta_{max}$ the tangent of the scanner aperture θ_{max}. The axial range where oblique projections are defined (if they are not recorded, they have to be completed) is L + 2.R.δ_{max}.
Let us note N_{sl} the number of transversal slices. The intrinsic axial sampling distance of the scanner is thus $\varepsilon_{ax} = L / N_{sl}$. Let us define a new axial range L' and a new number of axial samples N_{ax} as follows (figure 2):
N_{ax} is the smaller power of 2 such that:
L' / N_{ax} = L / N_{sl} = ε_{ax} in order to preserve the intrinsic axial sampling distance in the recorded projections.
L' ≥ L + 2.R.δ_{max} in order to take into account the missing oblique projections.

Let us note N_{rad} the number of radial samples in the sinograms (if needed, a re-sampling is performed in order to bring the number of samples to a power of 2).

The object is reconstructed on $(x_1,x_2,x_3) \in$ [-R, R] × [-R, R] × [-L'/2, L'/2] with N_{rad} samples in the x_1 and x_2 directions and N_{ax} samples in the x_3 direction.

The projections acquired in the cylindrical PET geometry are first rearranged in the two-plane geometry. The size $L_S \times L_Z$ and the number of samples $N_S \times N_Z$ in the two projection planes $\Pi_1=(O,x_2,x_3)$ and $\Pi_2=(O,x_1,x_3)$ are as follows:

$L_S = 4.R$

$N_S = 2.N_{rad}$

$L_Z = L'$

$N_Z = N_{ax}$

Along the transverse direction, the size of the projection planes is twice that of the original 3D projection data, in order to gather the projections up to either $1/|\cos\varphi| \leq 2$ or $1/|\sin\varphi| \leq 2$. The number of samples is also doubled in order to preserve the frequency range.

For a given direction $w=(\varphi,\theta)$, let us note $p*_{1w}$ the projection of the object on Π_1 with coordinates (S_1, Z_1) and $p*_{2w}$ the projection on Π_2 with coordinates (S_2, Z_2). Depending on φ, $p*_{1w}(S_1,Z_1)$ or $p*_{2w}(S_2,Z_2)$, is computed from $p(s,\varphi,x_3,\theta)$ using bi-linear interpolations in the s and z directions:

for $|\varphi| \leq \pi/4$ or $|\varphi| > 3\pi/4$ $p*_{1w}(S_1,Z_1) = p(S_1.\cos\varphi, \varphi, Z_1+S_1.\sin\varphi.\tan\theta, \theta)$, (17)

for $\pi/4 < |\varphi| \leq 3\pi/4$ $p*_{2w}(S_2,Z_2) = p(S_2.\sin\varphi, \varphi, -Z_1+S_2.\cos\varphi.\tan\theta, \theta)$. (18)

Using these specifications, the frequency steps in the object Fourier space will be: $\Delta\omega_1 = \Delta\omega_2 = 1/(2R)$, $\Delta\omega_3 = 1/L'$. In the 2D Fourier transform of the projections, the frequency steps will be: $\Delta\xi_S = 1/(4R)$, $\Delta\xi_Z = 1/L'$.

Remembering equations (13) and (15):

$$\hat{p}_{1w}(\xi_S,\xi_Z) = \frac{1}{|\cos\theta\cos\varphi|} \hat{f}(-\xi_S\tan\varphi - \frac{\xi_Z}{\cos\varphi}\tan\theta, \xi_S, \xi_Z)$$

$$\hat{p}_{2w}(\xi_S,\xi_Z) = \frac{1}{|\cos\theta\sin\varphi|} \hat{f}(\xi_S, -\frac{\xi_S}{\tan\varphi} - \frac{\xi_Z}{\sin\varphi}\tan\theta, \xi_Z),$$

it appears that, in the frequency domain, the samples of the 2D projection grid corresponding to $\xi_S = 2n.\Delta\xi_S = n.\Delta\omega_1 = n.\Delta\omega_y$ will fall exactly on the 3D object grid along two directions (ω_2 and ω_3 for Π_1, ω_1 and ω_3 for Π_2).
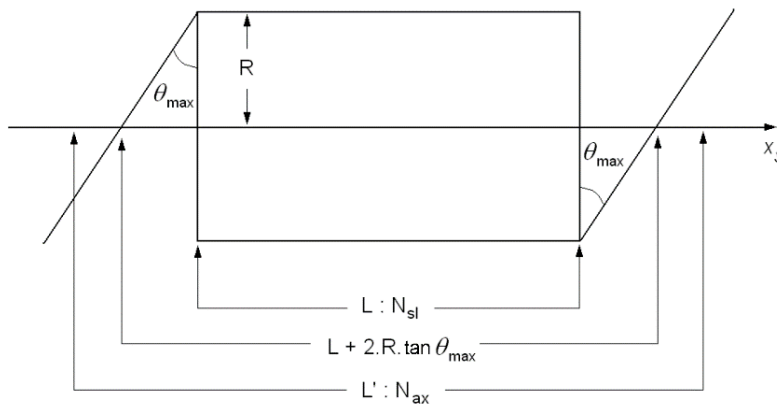

Figure 2. Explanatory diagram for the computation of the axial sampling N_{ax}.

The flow chart (figure 3) shows 2D (ω_1, ω_2) slices of the object 3D Fourier space ($\omega_3 = 0$). It illustrates, for each of the two projection planes, the position of the 2D grid points in the 3D space (①) and the corresponding points of the 3D grid that will be estimated (②).
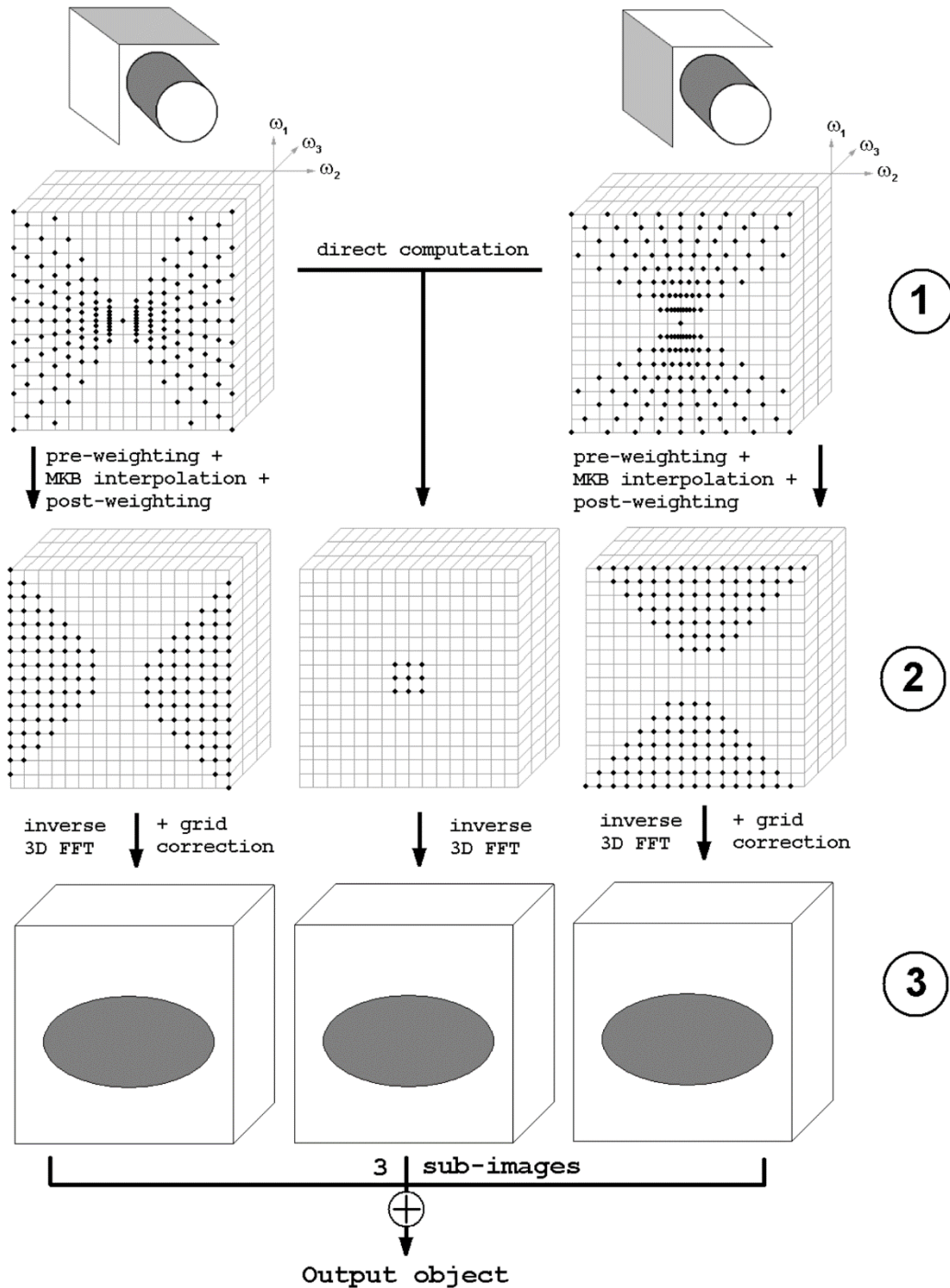

Figure 3. Flowchart of the image reconstruction steps.

The points corresponding to $(\omega_1,\omega_2) \in [-\Delta\omega_1\ \Delta\omega_1] \times [-\Delta\omega_2\ \Delta\omega_2]$ are processed directly (without having recourse to any interpolation) as they correspond to $\xi_S = 0$ or $\xi_S = 2.\Delta\xi_S$ for $(\theta = 0,\ \varphi = k.\pi/4)$. For other values of (ω_1,ω_2), the interpolation step is performed using a 1D modified Kaiser-Bessel (MKB) kernel characterized with the following parameters: Bessel function order $m = 0$, radius of the blob $a = 2.5$ pixels, and $\alpha = 15$.

A pre-weighting of the projection data spectrum is carried out in order to compensate the non-uniformity of the input grid density. A post-weighting of the image spectrum is also implemented to correct the effects induced by the finite size of the interpolation kernel. The weighting coefficients are pre-computed and stored on hard disk in limited space using symmetry relations. These kernel properties and weighting procedures are similar to those proposed by Matej *et al*. for 3D-FRP reconstruction [36].

The three subsets of the object 3D Fourier space allow the reconstruction of three sub-images after inverse 3D transform (③). Each of these sub-images is post-scaled using the inverse of the convolution kernel involved: for the first sub-image, the grid correction is performed in the x_1 direction; for the second, it is performed along the x_2 direction; and as the third involves no convolution, it needs no correction. The three sub-images are finally added in order to recover the object.

5. Performance study

Simulation data as well as patient data were produced using the characteristics of the Siemens Biograph PET scanner, a commercial scanner comprising 24 rings of 384 crystals per ring. The fields of view are 648 mm and 162 mm in the transaxial and axial directions, respectively. The ring radius is 412.5 mm and the maximum ring difference is 17. The axial compression (span) used was 7 or 1. Simulated sinograms were produced from known test volumes using analytical software dedicated to the computation of 3D sinograms from a simulated 3D distribution of radioactivity [40]. Acquisition artefacts such as Compton scattering or attenuation were not simulated. The times required to execute the algorithms were measured for the reconstruction of an unknown 3D radioactive distribution on a $128\times128\times64$ grid with a span of 7, corresponding to clinical settings. These times included the times required to read the sinograms and write the results on the disk. Using a 3 GHz personal computer, the processing times were 29 and 33 seconds for the FST-based algorithm and the two-plane method respectively. For comparison, on the basis of the same 3D configuration, the processing time was 2'51" for 3D filtered back-projection (3DRP) and 2'38" for 2D-OSEM coupled with FORE rebinning.

5.1. Resolution study

Even if the 3D reconstruction problem is not shift-invariant when the detector is a truncated cylinder, it is possible to compare the resolution properties of different reconstruction algorithms by estimating a "local" modulation transfer function (MTF) [41]. Therefore, in a $128\times128\times64$ grid, we simulated a 3D Gaussian distribution g, with a standard deviation of 3 mm, centered at the center of the field of view of the PET scanner. This distribution of radioactivity was used to simulate 3D sinograms. The reconstruction of these 3D sinograms provided a 3D distribution of radioactivity i. The "local" MTF was computed as the ratio of the 3D Fourier transform of the reconstructed image i to the 3D Fourier transform of the Gaussian

distribution *g*. Figure 4 shows the transaxial and axial MTFs for the two algorithms tested. The two algorithms provide the same curve for the axial MTF. Concerning the transverse MTF, the FST method shows slightly better results.
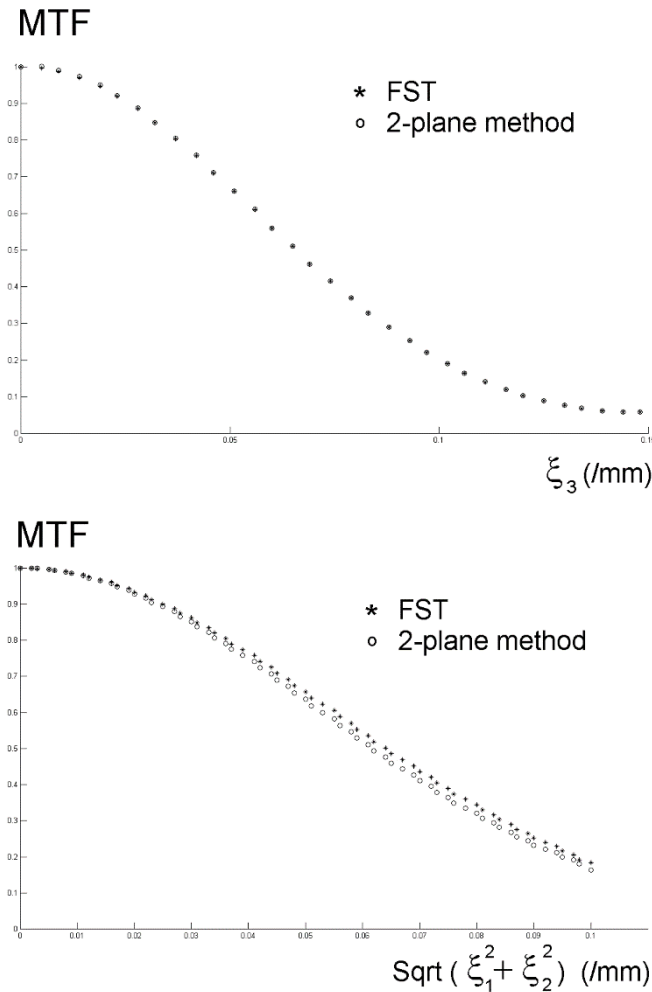

Figure 4. Transaxial (top) and axial (bottom) modulation transfer functions (MTF) at the center of the field of view for the usual implementation of the Fourier slice theorem and for the two-plane method. $\sqrt{\xi_1^2 + \xi_2^2}$ and ξ_3 are the transaxial and axial spatial frequencies.

To study line profiles on a noise-free reconstruction, a Derenzo-like phantom was simulated with 6 spheres with radii of 15 mm and 12 mm, 10 spheres with a radius of 9 mm and 15 spheres with a radius of 6 mm. The sphere to background ratio was 2. The volume was reconstructed onto a 128 x 128 x 64 grid. Figure 5 shows lines profiles through the central transaxial slice of this Derenzo phantom obtained with the two algorithms for a span set to 7 and when no noise is simulated. The top profiles correspond to the x_1 axis of the reconstructed slices, where objects with radii of 12 and 6 mm are intersected. The bottom ones corresponds to the x_2 axis which intersects the objects with radii of 15 and 9 mm. Besides the partial volume effects around the smallest spheres, these profiles show that the two algorithms performed rather similarly for resolution recovery.
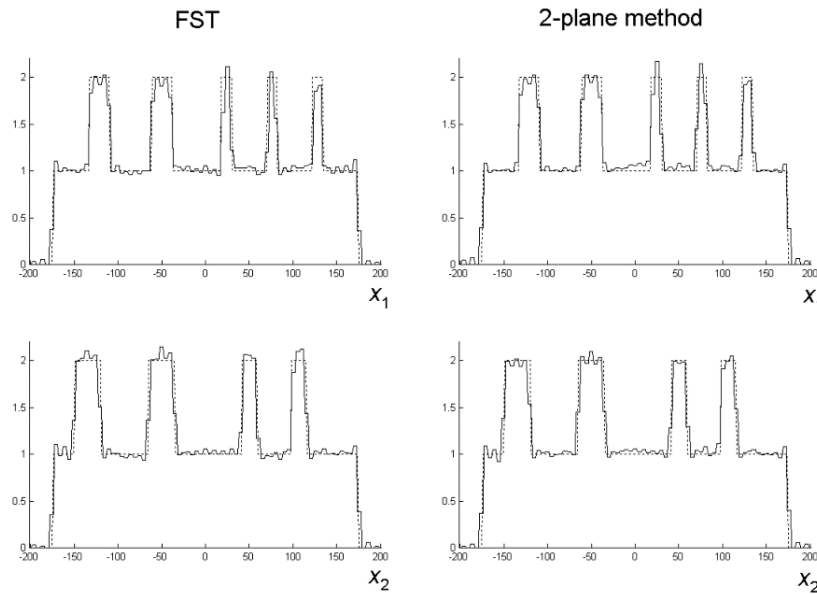
Figure 5. Central line profiles along the two transverse axes through the reconstructions of a
Derenzo-like phantom simulated with a span equal to 7 and without noise.

5.2. Noise properties

Noise properties were studied by computing the 3D sinograms of a 10-cm diameter uniform cylinder, extending along the entire axial field of view of the scanner (so that the length of the cylinder was 155.25 mm). Count rates in a range of 10-320 million events with a span 1 or 7 were simulated, without attenuation nor scatter. For the geometry of the PET and the uniform cylinder used, missing projection data existed if $|x_3| > 21$ mm or if $|x_3| > 9$ mm for a span set to 7 and 1, respectively. These missing data were estimated before reconstruction using the FOREPROJ algorithm [1,2].

For each reconstruction algorithm and for each transaxial slice, the coefficient of variation (CV) was evaluated as the ratio between the standard deviation and the mean pixel value within the entire cylinder slice. Figure 6 shows the CV measured with span 1 or 7 and a total net trues simulated corresponding to 10, 40 and 160 million events. As expected, the CV reached its minimum near the middle of the cylinder, where no projection data were missing. Whatever the configuration and the count rate, the CV measured was smaller with the two-plane algorithm than with the FST method (Table 1).

Figure 7 shows the evolution with the count rate (10 to 320 million events) of the mean CV (+/- standard deviation). The average was computed over the axial region where the shift-invariance was preserved. It clearly appears that the two-plane method allowed significant noise reduction compared with the FST method. This noise reduction reaches 25.2 +/- 0.4% for a span 1 and 17.4 +/- 0.5% for a span 7.

Table 1 compares the mean CV achieved using the two Fourier methods as well as a 2D-OSEM (16 subsets and 8 iterations, as specified by SIEMENS for routine clinical studies) coupled with FORE rebinning when reconstructing the cylinder with a span 7 and 10, 40 and 160 million events simulated.

Figure 8 shows the reconstructions of the previously described Derenzo-like phantom obtained with the two algorithms when 10, 40 and 160 million events were simulated with a span equal to 7. These images confirm that the signal to noise ratio was improved using the two-plane method compared with FST.
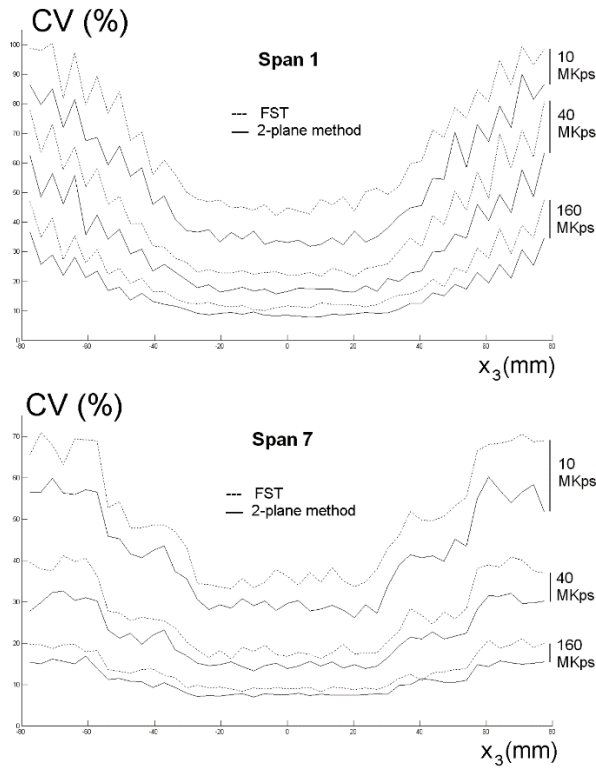
Figure 6. CV in the transaxial slices measured for the two algorithms in a cylindrical phantom with a span set to 7 (bottom) or 1 (top). Three counting rates are evaluated: 10, 40 and 160 Mkps.
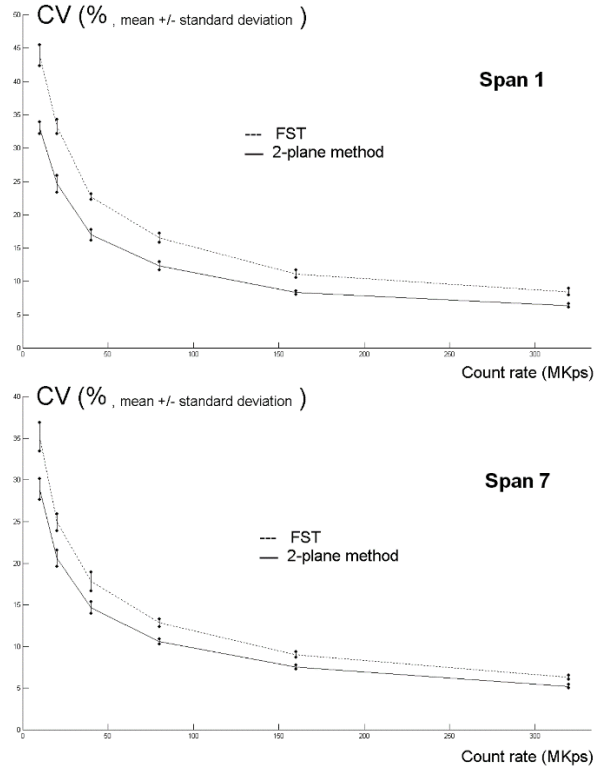
Figure 7. Evolution with the counting rate of the mean CV (+/- standard deviation) calculated in the axial range where the shift-invariance is achieved ($|x_3| < 9$ mm for span 1, $|x_3| < 21$ mm for span 7).

Last, a normal subject was injected with 5.5 MBq/kg of ^{18}FDG to record a PET brain study in a routine clinical setting using a Siemens Biograph PET scanner (span 7). The acquisitions were performed 30 minutes after injection. Three sets of projection data were recorded during 1, 3 and 10 minutes, respectively. This corresponded, respectively, to 20, 61 and 205 million counts (total net trues). The projections were processed using the FST-based algorithm and the two-plane method, after data completion using FOREPROJ, without correcting the attenuation artefacts (figure 9). Noise levels in the cortical tissues appeared less important for the slices reconstructed with the two-plane algorithm compared with those achieved using the FST-based algorithm.

Table 1. Comparison of the mean CV (+/- standard deviation) achieved in the shift-invariance region ($|x_3| < 21$ mm) using the FST method, the two-plane method, and FORE rebinning + 2D OSEM, for count rates of 10, 40 and 160 MKps and a span of 7.

	FST	2-plane method	FORE + 2D-OSEM
10 MKps	35.2 +/- 1.7	28.9 +/- 1.3	27.8 +/- 1.3
40 MKps	17.8 +/- 1.1	14.7 +/- 0.7	15.9 +/- 0.6
160 MKps	9.0 +/- 0.35	7.5 +/- 0.25	10.9 +/- 0.5

6. Discussion and Conclusion

Recent research dedicated to improving the numerical implementation of the 3D Fourier slice theorem has focused on the optimization of the interpolation procedure required by the DFM. These works, especially in the field of magnetic resonance imaging [42-44], have improved the gridding interpolation thanks to an optimization of the interpolating and weighting functions. They have been applied to 3D PET successfully [36]. In complement to this progress, only a few works have proposed to simplify the interpolation by using an appropriate representation of the projection data. A first step in this direction was made by Brasse et al., who considered the particular case of two perpendicular planar detectors parallel to the axis of the tomograph [15]. These authors provided two central section formulae that are equivalent to equations (12) and (15) of the present paper. However, the purpose of the planogram method was to propose fast and accurate back- (and forward-) projection operators using projection data acquired on planar detector arrays, without addressing the problem of interpolation in direct Fourier methods. In fact, processing the projection data of a usual cylindrical PET scanner onto one or several fixed planes can also be a way to provide a common grid for two directions in the 2D and 3D Fourier transforms, so that only a 1D (instead of 3D) interpolation is necessary. In a previous paper [39], we proposed using a single fixed plane to process the projection data. However, this algorithm requires the undesirable computation of 2D Fourier transforms of very large images because of the term $1/\tan(\theta)$ in equations (8). This explains the much longer computation time compared with the FST-based algorithm and the poor results of the validation study (not shown in this paper). Thus this method does not seem to be adapted to the geometry of routine clinical PET scanners, although it might be of interest in the case of large aperture scanners with projection data acquired for relatively high values of θ.

As shown in the first part of the present paper, the use of arbitrary fixed planes to process the projections can be an interesting framework to derive different direct Fourier algorithms for the reconstruction of 3D PET data. All these algorithms are based on the Fourier slice theorem, but the way they can be implemented and the complexity of the interpolation needed in the Fourier domain vary. Our study shows that the fixed planes chosen in this paper to represent the projection data provide a parameterization of the Fourier slice theorem that requires only a 1D interpolation in the Fourier domain to compute the 3D Fourier transform of the radioactive distribution. This property is likely to provide more accurate interpolations in the Fourier domain, especially for high spatial frequencies, thus resulting in a potential decrease in the noise in the reconstructed volume. The validation study confirms that the use of two orthogonal fixed planes provides similar resolution properties and an improved signal to noise ratio compared with direct implementation of the Fourier slice theorem. Moreover, the processing time remains similar to that of the FST-based method. Globally, the use of the two-plane method leads to signal to noise ratios that are similar to those achieved with the FST-based algorithm with up to twice as many count rates: when averaging over the tested range (10-320 MKps), the ratio between the count rates that provide similar SNR is 192% for a span 1 and 160% for a span 7 (which corresponds respectively to a reduction of 48% and 37.5% in the acquisition time). It also appears from Table 1 that the two-plane method brings a better signal to noise ratio than 2D-OSEM reconstruction, at least when the count rate exceeds a certain threshold. These preliminary results may be of clinical interest, especially when count rates are low, accelerated reconstruction procedures are needed (such as in dynamic PET studies), or patient irradiation must be decreased. Further clinical studies associating an optimized gridding interpolation and the use of two orthogonal fixed planes to process the projection data are now necessary. They will aim at determining, for a specific pathology, whether the gain in signal to

noise ratio described in this paper can actually make possible the reconstruction of similar volumes with fewer count rates than the usual fully 3D or rebinning algorithms used in commercially available PET systems.
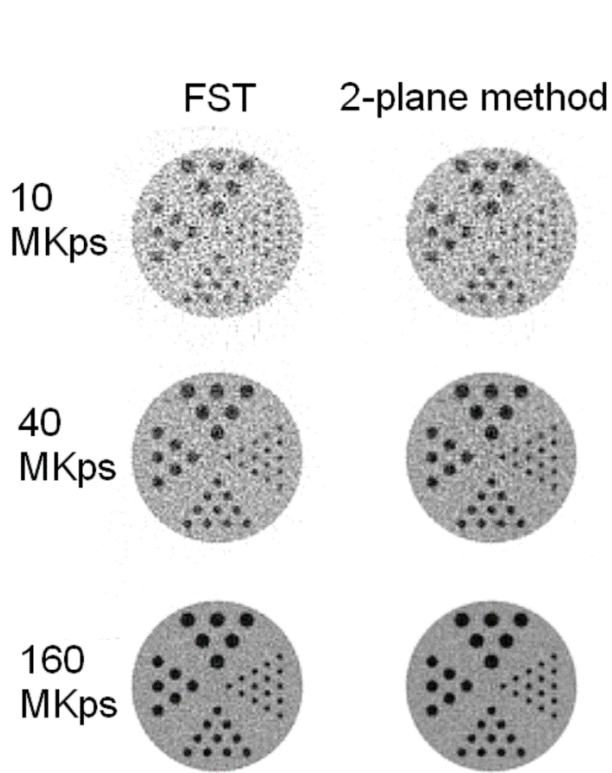

Figure 8. Reconstructions of a Derenzo-like phantom with 10, 40 and 160 million simulated events. The figure shows the results achieved with the two algorithms tested.
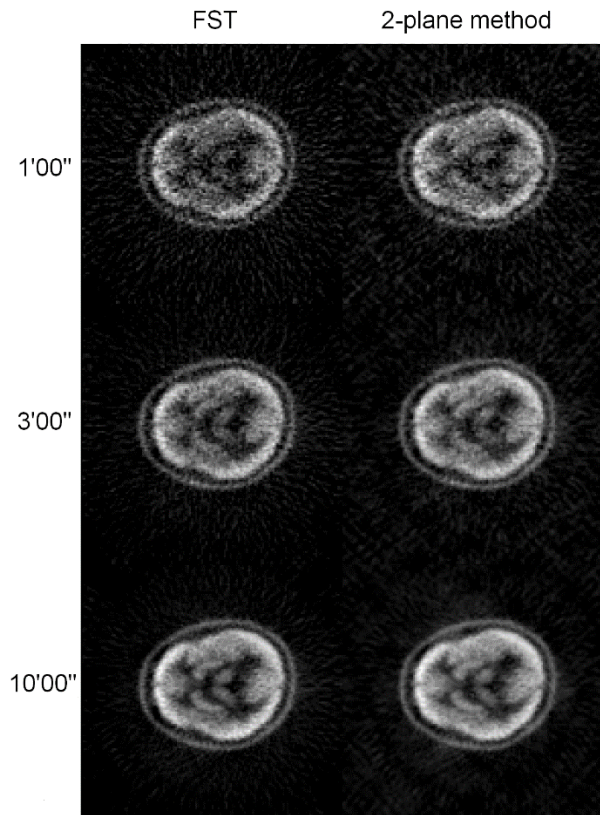
Figure 9. Reconstruction of a normal subject's brain PET study using the FST-based algorithm and the two-plane algorithm. The projection data were acquired over 1 minute (first line), 3 minutes (second line) and 10 minutes (third line).

Acknowledgment

References

[1]   M Defrise, P E Kinahan, D W Townsend, C Michel, M Sibomana and D F Newport 1997 Exact and approximate rebinning algorithms for 3-D PET data *IEEE Trans. Med. Imag.* **16-10** 145-158
[2]   X Liu, M Defrise, C Michel, M Sibomana, C Comtat, P E Kinahan and D W Townsend 1999 Exact rebinning methods for three-dimensional positron tomography *IEEE Trans. Med. Imag.* **18** 657-664
[3]   S Matej, J S Karp, R M Lewitt and A J Becher 1998 Performance of the Fourier rebinning algorithm

for the 3D PET with large acceptance angles *Phys. Med. Biol.* **43** 787-97

[4]   R M Lewitt, G Muehllehner and J S Karp 1994 Three-dimensional reconstruction for PET by multi-slice rebinning and axial image filtering *Phys. Med. Biol.* **39** 321-340

[5]   K Erlandsson, P D Esser, S E Strand and R L Van Heertum 1994 3-D reconstruction for a multi-ring PET scanner by single slice rebinning and axial deconvolution *Phys. Med. Biol.* **39** 619-629

[6]   V Sossi, M W Stazyk, P E Kinahan and T J Ruth 1994 The performance of the single-slice rebinning for imaging the human striatum as evaluated by phantom studies *Phys. Med. Biol.* **39** 369-380

[7]   E Tanaka and Y Amo 1998 A Fourier rebinning algorithm incorporating spectral transfer efficiency for 3D PET *Phys. Med. Biol.* **43** 739-746

[8]   M Defrise and X Liu 1999 A fast rebinning algorithm for 3D PET using John's equation *Inverse Problems* **15** 1047-1065

[9]   S S Orlov 1976 Theory of three dimensional reconstruction. 1. Conditions for a complete set of projections *Sov. Phys. Crystallogr.* **20** 312-314

[10] S S Orlov 1976 Theory of three dimensional reconstruction. II. The recovery operator *Sov. Phys. Crystallogr.* **20** 429-433

[11] M Defrise, P E Kinahan and C Michel 2003 Image reconstruction algorithms in PET" in "*Positron emission tomography. Basic sciences and clinical practice* P E Valk, D L Bailey, D W Townsend, M N Maisey, Ed., London: Springer Verlag 91-114

[12] C Axelsson and P E Danielsson Three-dimensional reconstruction from cone-beam data in $O(N^3 \log N)$ time *Phys. Med. Biol.* **39-3** 477-491

[13] J Hamil, C Michel and P Kinahan 2003 Fast PET EM reconstruction from linograms *IEEE Trans. Nucl. Sci.* **50-5** 1630-1635

[14] B De Man, S Basu 2004 Distance-driven projection and backprojection in three dimensions *Phys. Med. Biol.* **49-11** 2463-2475

[15] D Brasse, P E Kinahan, R Clackdoyle, M Defrise, C Comtat and D W Townsend 2004 Fast fully 3-D image reconstruction in PET using planograms *IEEE Trans. Med. Imag.* **23** 413-425

[16] J G Colsher 1980 Fully three-dimensional PET *Phys. Med. Biol.* **25** 103-115

[17] P E Kinahan and J G Rogers 1989 Analytic 3D image reconstruction using all detected events *IEEE Trans. Nucl. Sci.* **36** 964-968

[18] F C W Stearns, C R Crawford and H Hu 1994 Oversampled filters for quantitative volumetric PET reconstruction *Phys. Med. Biol.* **39** 381-388

[19] M Defrise, D W Townsend and R Clack 1995 Image reconstruction from truncated two-dimensional projections *Inverse Problems* **11** 287-313

[20] H Stark, J W Woods, I Paul and R Hingorani 1981 An investigation of computerized-tomography by direct Fourier inversion and optimum interpolation *IEEE Trans. Biomed. Eng.* BME **28-7** 496-505

[21] N Niki, R T Mizutani, Y Takahashi and T Inouye 1983 A high-speed computerized tomography image reconstruction using direct two-dimensional Fourier transform method *Syst. Comput. Controls* **14-3** 56-65

[22] C W Stearns, D A Chesler and G L Brownell 1990 Accelerated image reconstruction for a cylindrical positron tomography, using Fourier domain methods *IEEE Trans. Nucl. Sci.* **37** 773-777

[23] S Matej and I Bajla 1990 A high-speed reconstruction from projections using direct Fourier method with optimized parameters-An experimental analysis *IEEE Trans. Med. Imag.* **9-4** 421-429

[24] V M Tabei and M Ueda 1992 Backprojection by upsampled Fourier series expansion and interpolated FFT *IEEE Trans. Image Process* **1-1** 77-87

[25] M W Stazyk, J G Rogers and R Harrop 1992 Full data utilization in PVI using 3-D Radon transform

Phys. Med. Biol. **37** 689-704

[26] M Magnusson, P E Danielsson and P Edholm 1992 Artefacts and remedies in direct Fourier reconstruction *Proc 1992 IEEE Nucl. Sci. Symp. Med. Imag. Conf.,* Orlando, FL, USA, **2** 1138-1140

[27] J D O'Sullivan 1985 A fast sinc function gridding algorithm for Fourier inversion in computer tomography *IEEE Trans. Med. Imag* MI **4-4** 200-207

[28] J I Jackson, C H Meyer, D G Nishimura and A Macovski 1991 Selection of a convolution function for Fourier inversion using gridding *IEEE Trans. Med. Imag.* **10-3** 473-478

[29] H Schomberg and J Timmer 1995 The gridding method for image reconstruction by Fourier transform *IEEE Trans. Med. Imag.* **14-3** 596-607

[30] H Sedarat and DG Nishimura 2000 On the optimality of the gridding reconstruction algorithm *IEEE Trans. Med. Imag.* **19-4** 306-317

[31] S Matej and R M Lewitt 2001 3D FRP: Direct Fourier reconstruction with Fourier retroprojection for fully 3D PET *IEEE Trans. Nucl. Sc.* **48** 1378-1385

[32] J A Fessler and B P Sutton 2003 Nonuniform fast Fourier transforms using min-max interpolation *IEEE Trans. Signal Process.* **51-2** 560-574

[33] J I Jackson, C H Meyer, D G Nishimura and A. Macovski Selection of a convolution function for Fourier inversion using gridding *IEEE Trans. Med. Imag.* **10-3** 473-478

[34] P A Penczek, R Renka and H Schomberg 2004 Gridding-based direct Fourier inversion of the three dimensional ray transform *J. Opt. Soc. Am. A* **21-4** 499-509

[35] P J Beatty, D G Nishimura and J M Pauly 2005 Rapid gridding reconstruction with a minimal oversampling ratio *IEEE Trans. Med. Imag.* **24-6** 799-808

[36] S Matej and I G Kazantsev 2006 Fourier-based reconstruction for fully 3-D PET: optimization of interpolation parameters *IEEE Trans. Med. Imag.* **25-7** 845-854

[37] P R Edholm. and G T Herman 1987 Linograms in image reconstruction from projections *IEEE Trans. Med. Imag.* **6** 301-307

[38] P R Edholm and G T Herman, D A Roberts 1988 Image reconstruction from the linograms: implementation and evaluation *IEEE Trans. Med. Imag.* **7** 239-246

[39] D Mariano-Goulart and J F Crouzet 2005 A new reconstruction method in the Fourier domain for 3D positron emission tomography *CR. Physique* **6** 133-137

[40] C Comtat, P Kinahan, M Defrise, C Michel, C Lartizien and D Townsend 1999 Simulating whole-body PET scanning with rapid analytical methods *Proceedings of the IEEE Medical Imaging Conference*, Seattle, WA, USA

[41] M Defrise, A Geissbuhler and D W Townsend 1994 A performance study of 3D reconstruction algorithms for positron emission tomography *Phys. Med. Biol.* **39** 305-320

[42] C H Meyer, B S Hu, D G Nishimura and A Macovski 1992 Fast spiral coronary artery imaging *Magn. Reson. Med.* **28** 202-213

[43] D C Noll 1997 Multishot rosette trajectories for spectrally selective MR imaging *IEEE Trans. Med. Imag.* **16-4** 372-377

[44] J G Pipe and P Menon 1999 Sampling density compensation in MRI: Rationale and an iterative numerical solution *Magn. Reson. Med.* **41-1** 179-186